Methodology to investigate instantaneous and local transmembrane pressure within Rotating and Vibrating Filtration (RVF) module

Ming Cheng, Claude Le Men, Alain Line, Philippe Schmitz, Luc Fillaudeau

Methodology to investigate instantaneous and local transmembrane pressure within Rotating and Vibrating Filtration (RVF) module

Ming Cheng[1*], Claude Le Men[1,2], Alain Line[1,2], Philippe Schmitz[1,2], Luc Fillaudeau[1,2]

[1]TBI, Université de Toulouse, CNRS UMR5504, INRA UMR792, INSA, 31055, 135, avenue de Rangueil, Toulouse, France

[2]Federation de Recherche FERMAT (FR 3089), Université de Toulouse, CNRS, INPT, INSA, UPS, Toulouse, France

Abstract: Dynamic filtration exhibits high performances by generating wall shear stress (tangential to membrane) and pressure stress (normal to membrane) by the mechanical movements, such as rotating, oscillating or vibrating systems. Rotating and Vibrating Filtration (RVF) module includes rotating flat blades impellers which generate high and fluctuating shear stress and pressure at the membrane surface. To understand performances in turbulent regime and to optimise the operating conditions, global parameters (power consumption, pressure drop) and driving forces (mean, instantaneous and local pressure at the membrane surface) were characterised. For global approach, friction and mixing power in the RVF module were described by semi-empirical correlations. Euler number correlations were integrated based on feeding and mixing conditions. The balance between nominal power and thermal dissipation was reported. On the other hand, the mechanical power calculated with the empirical correlation of local shear stress was underestimated. For semi-local and local approaches, the local pressure at the membrane surface was measured with a specially designed and instrumented porous substrate. Mean radial pressure and core velocity coefficients were quantified versus flowrate and mixing rate. The core velocity coefficient decreases with mixing rate and radius up to a plateau value close to 0.6. For fluctuating component, pressure oscillation and its amplitude were treated by statistical analysis, probability distribution function and Fast Fourier transform. These methods show similar results with maximum fluctuating intensity between 15 and 30 Hz, which increase with radius. The maximum value can be obtained at the outer edge of the impeller with a relative standard deviation of over 25%. It indicates that the influence of pressure fluctuations should be carefully considered to enhance filtration performances. Pressure fluctuation distributions were accurately modelled by the convolution of periodic (sinusoid wave) and random (normal) functions. The area of intensive fluctuation was identified, in which periodic component accounts for 60% up to 97% of total energy input.

Keywords: Dynamic filtration; hydrodynamics; power consumption; core velocity coefficient; periodic and random pressure fluctuation.

Highlights:

- Semi-empirical correlations to estimate mixing and pumping powers;
- Determination of local core velocity coefficients and mixing pressure;

- Comparison of methods to analysis local fluctuating pressure;
- Reconstruction of pressure distribution with periodic and random functions.

*Corresponding author: Toulouse Biotechnology Institute, Bio & Chemical Engineering (TBI), Université de Toulouse, CNRS, INRAE, INSA, 135 avenue de Rangueil, 31077 Toulouse CEDEX 04, France
E-mail: cheng@insa-toulouse.fr (Ming Cheng)

Table of content

1 Introduction

Membrane separation technologies have attracted great attention and have been applied in a wide range of industrial applications: water treatment (drinking water and wastewater), food industry and biotechnology [1-4]. Traditional dead-end filtration is limited by cake formation at the membrane surface. A parallel flow relative to the membrane in cross-flow filtration mitigates the concentration polarisation and fouling by modifying the feeding flow direction. However, the increase of local shear stress is affected by the feeding flowrate, leading to an increase in pumping power. In comparison, dynamic filtration enhances both local shear (tangential) stress and pressure (normal stress) by the mechanical movement, such as rotating, oscillating or vibrating systems, which produce complex perturbations in the filtration system [5, 6]. Therefore, the hydrodynamics within the filtration unit needs to be identified in order to understand then to estimate the filtration performance [7-11].

High and stable permeate flux (J) is linked with the local shear rate γ at the membrane surface, and the empirical equation was promoted as $J = a\gamma^b$ [10, 12-17]. There is a break between two different regimes, above which the shear rate becomes more important as if the switch from laminar to turbulent regime [10, 12]. Among the rotating system, four different flow patterns were proposed due to the rotating disk [18]. When there is a narrow gap s between the rotor and the membrane, the boundary layers are merged together so that a continuous variation of tangential velocity in the gap. The limiting layer comes to separate in a larger gap, in which the fluid core is rotating at angular velocity $k \cdot 2\pi N$, k is the core velocity coefficient. Considering the mixing Reynolds number Re_{mixing}, the merged and separate boundary layers will result in different local shear rate expression at the membrane surface in the laminar or turbulent flow [7, 19-22].

There has been a lot of attention to improving k by increasing the roughness of the rotor or the modification of the rotating system in order to intensify shear-enhanced filtration. The flow between a stationary and a rotating disk system was early studied by Wilson et al., who indicated a k value of 0.31 for the two infinite disks [23]. A similar result obtained by Bouzerar et al. [7] showed a k value is 0.32 with a 3 mm gap of Plexiglas disk in the turbulent regime. By changing the gap, number and/or width of vans, k increases from 0.44 for a smooth disk to 0.84 for an 8 mm gap and equipped with eight pairs of 6 mm vans [7, 12, 16, 24, 25]. With the same theory, a three-blade impeller at a 3 mm gap in the RVF module gave a k equal to 0.71 [8].

The contribution of rotation is not only the high shear rate to limit the cake layer, but also the increased transmembrane pressure. Fillaudeau et al. [9] found at a 50 Hz mixing rate, the additional pressure generated by mixing could reach up to 900 mbar with the RVF module. However, this mean pressure fluctuates on the time scale, limited knowledge about that instantaneous pressure is reported in the literature [18]. Therefore, it is necessary to investigate the fluctuating pressure at the membrane surface during the rotor rotation, which requires fast and accurate measurements. The physical signal of the unsteady pressure contains enough information about the fluid flow with respect to different operating conditions [26-30].

Stress-enhanced filtration is defined as the mechanical movement to cause a high shear rate at the membrane surface. This technology will generate unsteady flow and result in the fluctuations of transmembrane pressure. In the present study, the RVF module equipped with a specially designed cell to achieve accurate measurements of the instantaneous pressure at the membrane surface. The characteristics of fluctuating pressure were analysed on time and frequency domain for different operating conditions under turbulent flow, then compared with the model established by a sinusoid wave and random component. Another focus of this work is the power consumption of the loop. The empirical relationships about the global pressure drop of RVF and the net power of the rotor were established, respectively, allow an easy estimation for the energy demand for the processing.

2 Materials and methods

2.1 Experimental set-up and instrumentation

2.1.1 RVF module

The lab-scale RVF module [8, 11] (Fig. 1a, and b) consists of two filtration cells with a volume of 0.2 L. Four disk membranes (0.048 m^2 filtration area per membrane) can be mounted on the porous substrates, which collect permeate drained to lateral ducts. Each cell includes two crown membranes with a gap of 14 mm, between which are located a three-blade impeller rotates with the central shaft (Fig. 1e). And it is driven by a motor that can be operated up to 50 Hz. The feeding fluid comes inside RVF from the inlet at the bottom and flows through the module along with the central shaft, finally leaves from the retentate outlet at the top.

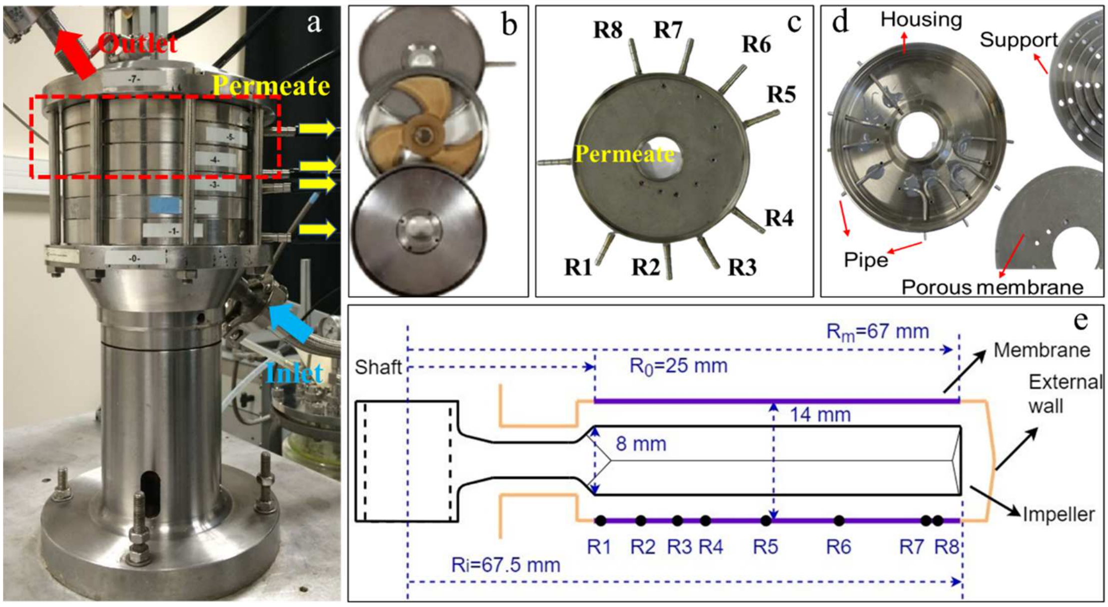

Fig. 1 Schematic diagram of Rotating and Vibrating Filtration module. (a) RVF module; (b) one dismantled filtration cell; (c) and (d) home designed and instrumented porous substrate for local

pressure measurements; (e) configuration of filtration cell.

In Fig. 1c and d, a home designed and instrumented porous substrate was used to measure the local pressure at the membrane surface. Eight pressure taps (2 mm) were connected to stainless tubes, with one extremity welded to the porous support and the other extremity located on the outer cell wall. The pressure taps were distributed between 26.2 mm (R1) up to 64.9 mm (R8), as indicated in Table 1.

Table 1 Radial distribution of pressure taps at the membrane surface (porous substrate).

Radial position	Radius (mm)	Radial position	Radius (mm)
R1	26.2	R5	45.3
R2	29.3	R6	53.9
R3	34.8	R7	63.4
R4	38.2	R8	64.9

2.1.2 Experimental set-up

The experimental set-up is displayed in Fig. 2; it includes a feed tank, a circulation loop and the RVF module Fig. 1. In the circulation loop, water was pumped from a double-jacket tank (2L), including thermal regulation at flowrate ranging from 50 to 300 L/h. Flowrate was controlled by a volumetric pump (Pump, TUTHILL, PM8014, 3800 rpm, 169 W) and acquired with a mass flowmeter (MF, KROHNE, Optimass 70000 S06), it enabled the measurement of mass flowrate (0/900 kg/h, ±0.1% liquid, ±0.1% gas), density (500/2000 kg/m^3, ±2 kg/m^3) and temperature (0/130 °C, ±1 °C, was associated with outlet temperature). The inlet temperature was recorded from the conductivity sensor, Cond (Conductimetre Conducell 4USF PG 325, -20/150 °C, ±0.5 °C), in the feeding tank. The back pressure in RVF was adjusted by a counter-pressure valve coupled with a pressure gauge (PG, 0/4 bar) and a relative pressure sensor (PR1, Bourdon-Haenni Y913, 0/6 bar, ±0.2% full scale) located in the outlet. Before the experiments, the back pressure was maintained at 300 mbar to avoid cavitation caused by the high mixing rate. A Tachymeter (Tachymeter Testo 460, 100-30000 rpm) was used to adjust the mixing rate (N) from 0 to 50 Hz. Both current (CU, Ammeter, LEM Co. AC current transducer AT-B10, 0/20 A) and tension (TEN, Voltmeter, SINEAX U 504 31 LD, 0/250 V) of the motor were recorded for all the conditions. The differential pressure sensors (DP, HONEYWELL-STD 120, 0/1 bar, ±0.0375% full scale) were used to determine the pressure drop and local pressure of RVF. The relative pressure (PR2, Killer, -1/+1 bar, ±0.2% full scale, maximum acquisition frequency 5 kHz) was measured at the membrane surface.

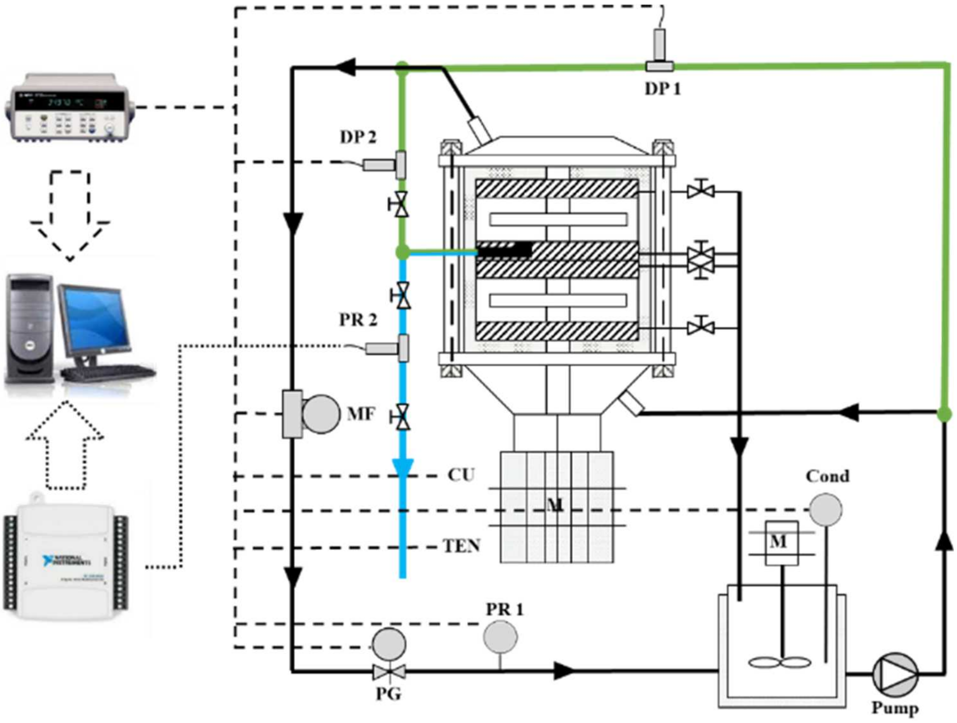

Fig. 2 Experimental set-up. Mean and instantaneous pressure measurements are illustrated by green (differential pressure, DP1 and DP2) and blue (relative pressure, PR2) lines.

2.1.3 Experimental measurement and data acquisition

Two types of measurements were performed without permeate: (i) global measurement and (ii) instantaneous and local pressure measurement. Tap water (25±5 °C) was used as feed fluid with 4 flowrates ranging from 50 to 300 L/h. The instantaneous and local pressure was measured at 8 radii from R1 to R8, and the 15 mixing rates from 0 to 50 Hz.

Global measurements along the circulation loop correspond to differential pressure (DP1, located between the inlet and outlet; DP2, installed between the local radius and outlet), flowrate, temperature, current and tension. All the sensors were connected to a data acquisition system (Agilent 34972A, Agilent Technologies, Loveland, USA) with a multiplexer acquisition card (34901A, 20 channels). After 2 min stabilisation, all electrical signals were recorded at 5 s intervals for 3 min.

Instantaneous pressure was measured with PR2 (shown in the blue line in Fig. 2) at 1000 Hz, connected to the local radius. The pressure signal was recorded with NI USB-6009 (National Instruments, USA, 1 kHz) at a sampling frequency of 1000 Hz for more than 40 s.

2.2 Global and semi-local analysis: pressure drop, mixing pressure and core velocity coefficient

For the dynamic filtration devices, global and mean local values of pressure, velocity, and shear rate in the filtration cell have been described previously [8, 9, 11, 31]. From a global standpoint, RVF modules can be assimilated to a hydraulic singularity generating a pressure drop and as a mixing device. Linear pressure drops in the RVF module (ΔP_{RVF}) is attributed to the friction loss, which can be expressed by Euler dimensionless number, Eu, given by Eq. (1).

$$Eu = \frac{\Delta P_{RVF}}{1/2\rho u^2} \tag{1}$$

where ΔP_{RVF} was measured by DP1, ρ is the fluid density, u is the velocity at the inlet of RVF module. The Reynolds number for feeding ($Re_{feeding}$) and mixing (Re_{mixing}) are defined as follows:

$$Re_{feeding} = \frac{\rho d u}{\mu} \tag{2}$$

$$Re_{mixing} = \frac{\rho N d_i^2}{\mu} \tag{3}$$

where d is the inlet diameter (12 mm), d_i is the diameter of the rotating impeller, μ is dynamic viscosity, N represents the mixing rate of the impeller.

Two methods were used to measure power consumption. The first case is given by the current and tension of the motor. The electrical power needs to drive the shaft were measured without fluid, which is considered shaft loss. Thus, the net power Φ_N consumed by the rotating impeller is equal to the difference between total power and shaft losses [16]. It can be described by Power number Np in Eq. (4). Another case is achieved by the thermal dissipation Φ_T of water in the filtration module and given by Eq. (5).

$$Np = \frac{\Phi_N}{\rho N^3 d_i^5} \tag{4}$$

$$\Phi_T = \rho Q_F C_P (T_{inlet} - T_{outlet}) \tag{5}$$

where T_{inlet} and T_{outlet} are the inlet and outlet temperature, respectively, Q_F is the feeding flowrate, and C_P is the specific heat capacity of water.

Since the impeller is installed with a narrow gap to the membrane, assuming the inviscid core layer rotates at an angular velocity of $k \cdot 2\pi N$. According to Bernoulli's equation in Eq. (6) [7], the mean local pressure $\bar{P}(N,r)$ at the membrane surface equals the sum of P_0 and ΔP_{mixing}. P_0 is the pressure at the centre of membrane or be given by the pressure when the absence of mixing, while ΔP_{mixing} is the additional pressure driven by the rotating impeller.

$$\bar{P}(N,r) = P_0 + \Delta P_{mixing} = P_0 + \frac{1}{2}\rho(k \cdot 2\pi N)^2 r^2 \tag{6}$$

where r is the radius at the membrane surface.

2.3 Local analysis: instantaneous pressure

Three blades impeller was used in the experiments, which result in a 150 Hz signal when rotating at 50 Hz. The instantaneous pressure has been measured with a 1000 Hz sampling frequency. Considering the pressure fluctuations as a result of vibrating flow, the instantaneous pressure can be expressed as Eq. (7), with $\bar{P}(N,r)$ and $\tilde{P}(N,r,t)$ represent the mean and fluctuating pressure, respectively. Fig. 3a and b illustrate the time evolution of absolute pressure and its fluctuating component.

Pressure oscillation and its amplitude can be treated by (i) statistical analysis, SA; (ii) probability distribution function, PDF and (iii) Fast Fourier transform, FFT.

$$P(N,r,t) = \bar{P}(N,r) + \tilde{P}(N,r,t) \tag{7}$$

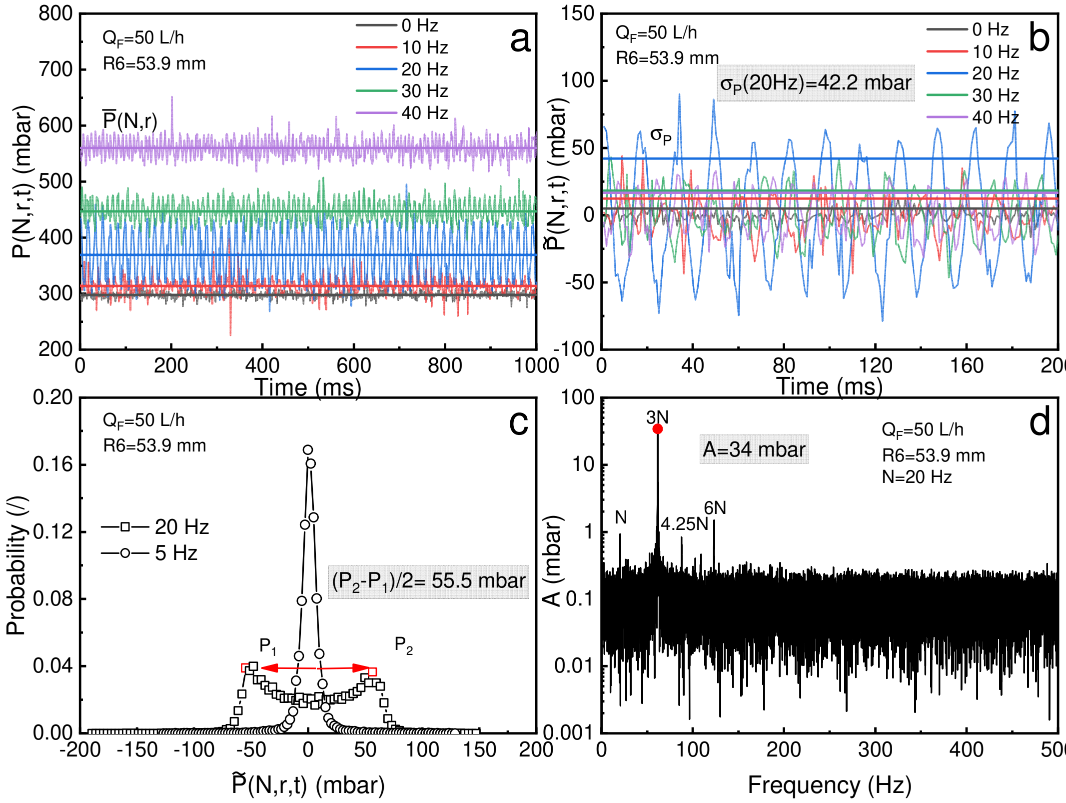

Fig. 3 The spectrum of instantaneous pressure and data treatment. (a) instantaneous and mean pressure; (b) fluctuating pressure and its standard deviation; (c) probability analysis at 5 and 20 Hz; (d) fluctuating pressure on frequency domain at 20 Hz.

2.3.1 Statistical analysis

The standard deviation of the signal has been widely accepted to quantify fluctuating intensity [29, 32, 33]. In our condition, a total number of sampling ($m=2^{15}$) is acquired at a constant time interval (1 ms), as illustrated in Fig. 3b. The mean pressure $\bar{P}(N,r)$ and standard deviation σ_P are expressed as the moment of first order and the square root of the central moment of second order, respectively. Their mathematical definitions for continuous and discrete functions are given in Eq. (8) and (9). The coefficient of variation, β is defined as the ratio between σ_P and $\bar{P}(N,r)$, and give the relative standard deviation.

$$\bar{P}(N,r) = \frac{1}{T}\int_0^T P(N,r,t)dt \approx \frac{1}{m}\sum_{i=1}^{m} P(N,r,t_i) \tag{8}$$

$$\sigma_P{}^2 = \frac{1}{T}\int_0^T (P(N,r,t) - \bar{P}(N,r))^2 dt \approx \frac{1}{m}\sum_{i=1}^{m}(P(N,r,t_i) - \bar{P}(N,r))^2 \tag{9}$$

$$\beta = \frac{\sigma_P}{\bar{P}(N,r)} \times 100\% \tag{10}$$

The normalised central moment of the third order, known as skewness (*S*), determines the symmetry of signal in the probability distribution, and zero means a symmetrical distribution.

$$S = \frac{1}{T{\sigma_P}^3}\int_0^T (P(N,r,t) - \bar{P}(N,r))^3 dt \approx \frac{1}{m\sigma_P^3}\sum_{i=1}^{m}(P(N,r,t_i) - \bar{P}(N,r))^3 \tag{11}$$

The flatness (*F*) is represented by the normalised central moment of the fourth order, indicates the sharpness of distribution.

$$F = \frac{1}{T{\sigma_P}^4}\int_0^T (P(N,r,t) - \bar{P}(N,r))^4 dt \approx \frac{1}{m\sigma_P^4}\sum_{i=1}^{m}(P(N,r,t_i) - \bar{P}(N,r))^4 \tag{12}$$

2.3.2 Probability distribution function

Another method for obtaining the intensity of fluctuating pressure can be carried out with probability analysis [26]. By subtracting the average pressure, the deviation signal is divided into 100 classes considering 2^{15} of raw data. The probability of each class can be calculated based on its occurrence. In Fig. 3c, the probability is illustrated against the fluctuating pressure. The unimodal (dominant random contribution, *cf.* §3.3.4) distribution of probability is observed at 5 Hz while extended to bimodal (dominant periodic contribution) at 20 Hz. These PDF widths are defined by peak-to-peak differences divided by 2, $(P_2-P_1)/2$, finally resulting in the pressure intensity of 55.5 mbar at 20 Hz.

2.3.3 Fast Fourier transform (FFT)

The Fast Fourier Transform decomposes a signal into a series of sinusoid waves to be analysed and given by the frequency domain signal. It has been used to extract information about fluctuation (amplitude and frequency) from the time-series signal. Continuous and discrete Fourier transform can be represented by:

$$P(f) = \int_{-\infty}^{+\infty} \tilde{P}(N,r,t)e^{-j2\pi ft}dt \approx \sum_{i=0}^{m-1}\tilde{P}(N,r,t_i)e^{-\frac{j2\pi fi}{m}}, \quad f = 0,1,\ldots,m-1 \tag{13}$$

where $\tilde{P}(N,r,t_i)$ is the deviation of pressure at point *i*, *f* is the frequency. This formula is associated with the complex plane, composed of real and imaginary parts, and its amplitude (*A*) can be expressed as follows:

$$A = \frac{2}{m}\sqrt{P(f)^2} \tag{14}$$

The time-dependent fluctuating pressure can be converted into the frequency domain with FFT [27-30, 32]. 2^{15} sample points were chosen to get a sufficient precision of the fluctuated signal. The amplitude and frequency, driven by the rotating impeller, are discussed in the next part. Fig. 3d shows the typical result of FFT at 20 Hz. The peak amplitude (*A*) is defined as the intensity of fluctuation pressure.

2.3.4 Reconstruction of PDF with periodic and random functions

The fluctuating signal consists of two parts: periodic and random contributions (Table 2). The periodic signal can be simplified as a single sinusoidal fluctuation with $f=3N$, whose intensity is determined by the amplitude A. Since only one peak is considered, the A presented here is higher than the FFT amplitudes at the same frequency. The random signal conforms to a normal distribution with a zero mean, and σ denotes the standard deviation. The energy input in each contribution is given by their root mean square (RMS).

Table 2 Signal decomposition into periodic and random contributions ($P_P(t)$: periodic signal, $P_R(t)$: random signal, A: amplitude, f: frequency, φ: phase, σ: standard deviation, $E_P(x)$ and $E_R(x)$ are the PDF.).

Contribution	Function	Parameters	PDF (mbar^{-1})	Energy input (mbar)
Periodic	$P_P(t) = Asin(2\pi ft + \varphi)$	$A, f=3N, \varphi$	$E_P(x) = \frac{1}{\pi\sqrt{A^2 - x^2}}$	$A/\sqrt{2}$
Random	$P_R(t) \sim N(\bar{x}, \sigma^2)$	$\bar{x} = 0, \sigma$	$E_R(x) = \frac{1}{\sigma\sqrt{2\pi}} e^{-\frac{1}{2}(\frac{x-\bar{x}}{\sigma})^2}$	σ

In theory, the continuous model of pressure fluctuation distribution results from the convolution of *EP(x)* with *ER(x)* as reported in Eq.(15). Comparison between experimental data and model is realised by identifying amplitude, A for periodic component and standard deviation, σ for random term. Considering the statistical convergence, phase lag has no effect on PDF building (*cf.* §3.3.1). Both optimal parameters, A and σ are obtained by minimising the cumulative error function, Δ with Eq.(16), thanks to Excel solver (Suite Office Microsoft 2013, Excel, GRG non-linear) for each operating condition. Fig. 4 illustrated the experimental and simulated PDF at R6 and 20 Hz.

$$PDF = E_P(x) * E_R(x) \tag{15}$$

$$\Delta = Min\left(\sum_{i=0}^{100}\sqrt{(Experiment - Model)^2}\right) \tag{16}$$

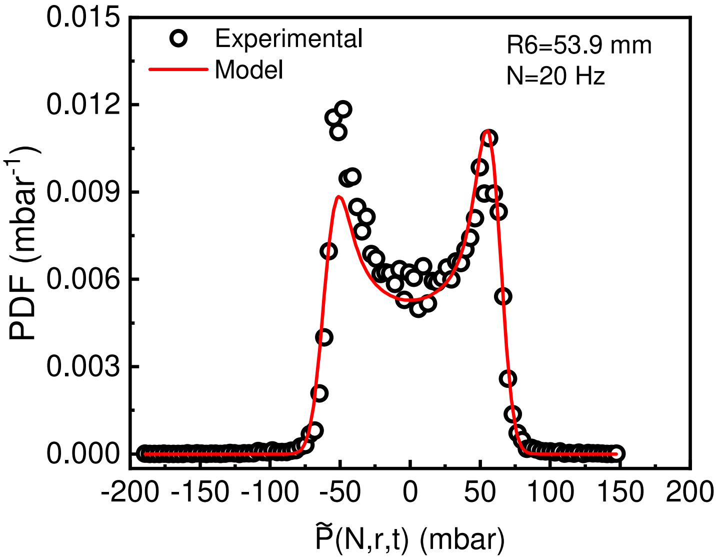

Fig. 4 PDF at 20 Hz. Model reconstruction of PDF with periodic and random functions.

3 Results and discussion

3.1 Global approach

3.1.1 Pressure drops (Eu vs Re)

At the process scale, the RVF module can be identified as a hydraulic singularity (generating pressure drop) or a confined mixing device (power consumption). The evolution of Euler number versus feeding ($800<Re_{feeding}<9000$) and mixing ($10^3<Re_{mixing}<10^6$) Reynolds numbers are shown in Fig. 5a. In the absence of rotation, *Eu(N=0)* shows a decrease with increasing $Re_{feeding}$ from 41 to 34, which tends to be negligible at a higher mixing rate. That is consistent with the friction curve established by Fillaudeau et al. [9] in the turbulent flow regime. By increasing the mixing rate, *Eu* rises dramatically with Re_{mixing}; the magnitude of Eu increase is inversely proportional to the flowrate.

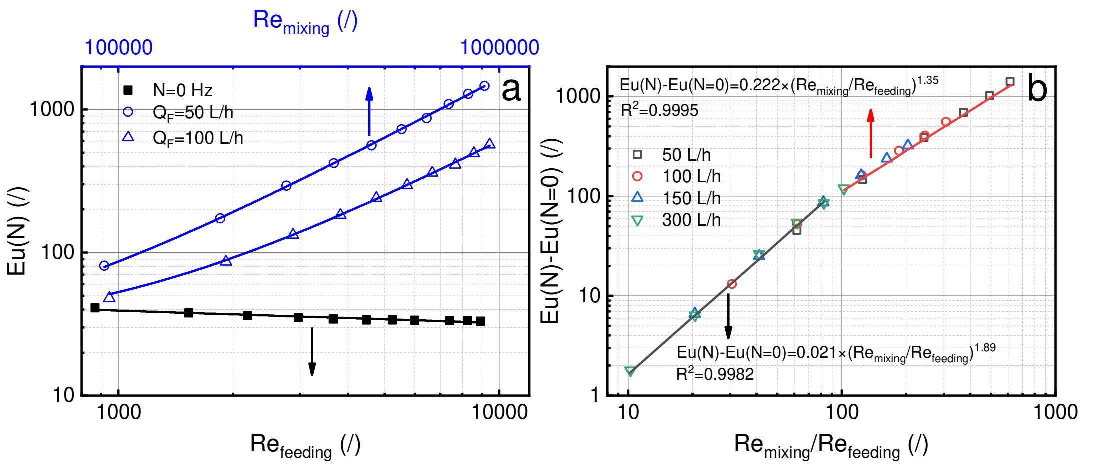

Fig. 5 Friction curve. (a) the evolution of Euler number versus feeding and mixing Reynolds number; (b) the regressions of Euler number increment in diverse mixing rate and flowrate.

For process engineer and scaling, it appears useful to establish simple semi-empirical correlations to estimate the pressure drop and power consumption in such a module. Subtracting *Eu(N=0)*, the Euler number increment is plotted as a function of $Re_{mixing}/Re_{feeding}$ in Fig. 5b. Two domains are found by the regression of data, giving two semi-empirical correlations as:

$$Eu_{(N)} - Eu_{(N=0)} = 0.021 \times (\frac{Re_{mixing}}{Re_{feeding}})^{1.89} \qquad \frac{Re_{mixing}}{Re_{feeding}} < 100 \tag{17}$$

$$Eu_{(N)} - Eu_{(N=0)} = 0.222 \times (\frac{Re_{mixing}}{Re_{feeding}})^{1.35} \qquad \frac{Re_{mixing}}{Re_{feeding}} \geq 100 \tag{18}$$

These correlations have been validated for the feeding and mixing condition ($10^3 < Re_{feeding} < 1.2 \times 10^4$, and $0 < Re_{mixing} < 10^6$).

3.1.2 Power consumption (Np vs Re_{mixing})

Power consumption is a critical issue in evaluating the overall performance of a rotating dynamic filtration device. For RVF module, the total energy consumption includes the pumping and mixing power. Assuming the highest feeding flowrate at 300 L/h and back pressure of 300 mbar, the pumping power can be estimated to be 2.5 W. This can be negligibly in comparison to the mixing power for $N \geq 20$ Hz ($\Phi_N \approx 400$ W at 50 Hz).

In the small-scale filtration module, the mixing power without load (P_f) cannot be neglected due to the friction of the shaft. In the present case, the contribution of the power consumed by the impeller is inferior to P_f at the mixing rate below 20 Hz. As shown in the power consumption curve (Fig. 6a), the grey area indicates the excessive mechanical losses in the rotating shaft. Np is independent of Re_{mixing} when $N \geq 20$ Hz, and remains around 0.1.

In Fig. 6b, the mixing power was estimated thanks to 3 approaches: (i) power consumption curve (Φ_N), (ii) thermal balance (Φ_T) and (iii) investigation of local shear stress (Φ_M). Power consumption and thermal balance show a good agreement, and the thermal dissipation of fluid constitutes 87.73% of the electrical power consumed by the mixing, the rest of which may be attributed to the dissipation of the cell wall. In a turbulent regime, the boundary layers merge together at a narrow gap (3 mm), and the local shear stress τ on the rotating disk in Eq. (19) illustrates the linear relation with $N^{1.75}$ [22, 34]. As mentioned by Brou et al. [16], the mechanical power Φ_M generated by the friction force on the plate disk is calculated by Eq. (20). In our case, Φ_M varies linearly with the nominal power and is underestimated (24.06%). If the impeller surface area is considered, this ratio reduces to 12%. It demonstrates that the local shear stress on the blades only corresponds to a minor fraction of the torque. The major contribution of driving force contributes to the pressure difference between the leading and trailing edge of blades, which need to be further investigated.

$$\tau = 0.008\rho^{0.75}(2\pi N \cdot r)^{1.75}(\frac{\mu}{S})^{0.25} \tag{19}$$

$$\begin{aligned}\Phi_M &= 2\int_{R_0}^{R_i} 2\tau\,(2\pi N\cdot r)(2\pi r)dr \\ &= 6.632\rho^{0.75}\left(\frac{\mu}{s}\right)^{0.25}\left(R_i^{4.75}-R_0^{4.75}\right)N^{2.75}\end{aligned} \tag{20}$$

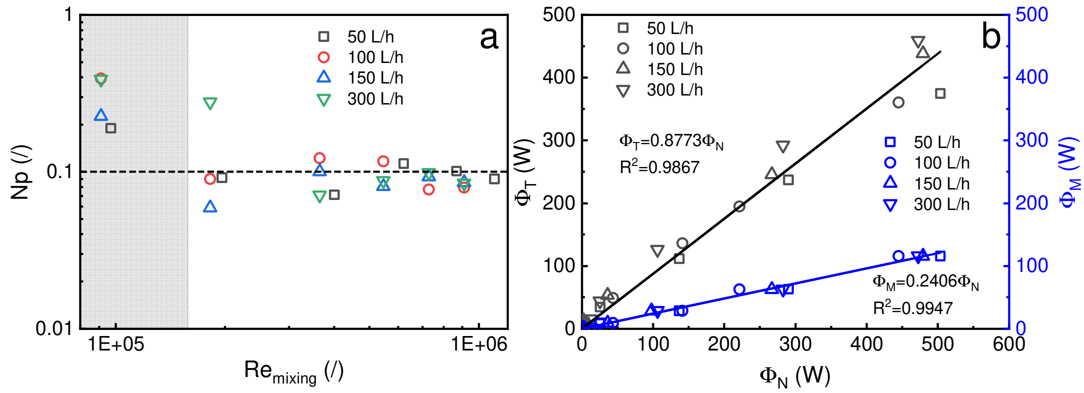

Fig. 6 Power consumption curve. (a) the variation of Power number versus mixing Reynolds number; (b) thermal dissipation and mechanical power versus net electrical power.

3.2 Semi-local approach: analysis of core velocity coefficient

The local pressure at the membrane surface was measured at different radius (26.2 to 64.9 mm), mixing rates (0 to 50 Hz) and flowrates (50 to 300 L/h). According to Eq. (6), the mixing pressure is plotted in Fig. 7, and parabolic variation with the mixing rate can be observed. At 50 L/h, the mixing pressure rises as the radius increases in terms of impeller tangential velocity. By increasing the feeding flowrate, a small increase in pressure can be observed due to the velocity generated by feeding.

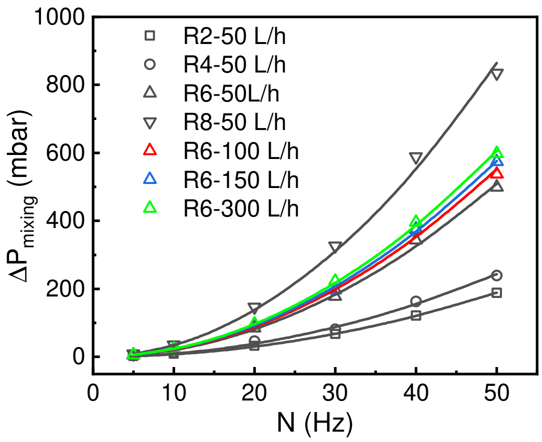

Fig. 7. The evolution of mixing pressure as a function of radius and feeding flowrate.

Fig. 8a shows the regression of mixing pressure as a function of N^2r^2 from 50 to 300 L/h. The great correlation indicates a core velocity coefficient equals to 0.65, which is slightly lower than 0.71, reported by Fillaudeau et al. [9]. Previously, the mixing pressure at a defined radius was measured with the permeable crowns. With large gaps (5 mm) in the annular cavity, the k value was overestimated using the mean radius. Fig. 8b demonstrates the *k* values vary with radius, flowrate and mixing rate. The highest *k* values are observed at R1. They increase by 21% with flowrate between 50 and 300 L/h, while only 3% at the boundary (R8). The flowrate is more important at the inlet due to the small cross-section related to high radial velocity. Similar to the rotating disk module [7], the *k* value decreases with the increment of radius and further improves when reaching the edge of the disk. These variations with impeller are higher than the full disk, reaching 10% at 300 L/h, which may be explained by the shape of the blades.

The ideal conditions based on a full disk system assumes that mean local velocity (horizontal) results from radial and tangential velocities. $U_r(r)$ is determined by feeding flowrate and local cross-section, and $U_\theta(r)$ by mixing rate and core velocity coefficient (Eq. (21)).

$$U_{r\theta}{}^2(r) = (k_{theo}2\pi Nr)^2 + \left(\frac{Q_F}{2\pi rs}\right)^2 = \left(k_{exp}2\pi Nr\right)^2 \tag{21}$$

For example, the radial velocity at R1 is around 0.028 m/s for 50 L/h, and the impeller angular velocity is equal to 0.823 m/s at 5 Hz. Under this condition, the ratio between radial and angular velocities is limited to 3%. At the highest feeding flowrate (300 L/h), this ratio reaches more than 20%. It indicates that the contribution of feeding is more important with the lowest radii and mixing rates, as described by Eq. (21). As shown in Fig. 8b, the *k* values tend to decrease with the rise of mixing rate and radius. In our conditions, a plateau value (~0.6) appears for a radius superior to 45 mm. However, the slight k increase is not clear yet.

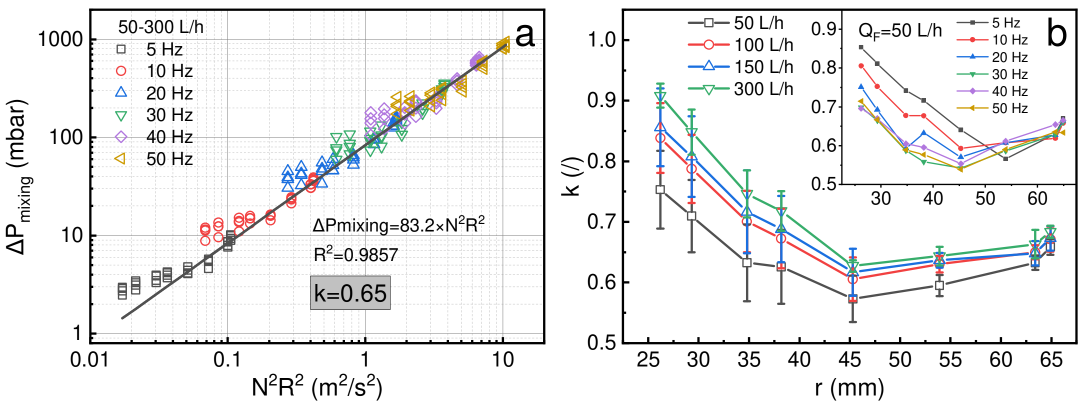

Fig. 8 The determination of the core velocity coefficient. (a) the regression of mixing pressure at the flowrate ranging from 50 to 300L/h; (b) the evolution of core velocity coefficient versus radius, flowrate and mixing rate.

3.3 Local approach: Instantaneous pressure at the membrane surface

3.3.1 Statistical analysis

As preliminary verification, the evolutions of $\bar{P}(N,r)$, σ_P, S and F as a function of sampling number (Fig. 9) demonstrate that statistical convergence of raw data is reached for *m>1000*. The sampling number *m* (2^{15}) may be sufficient to be analysed with the following methods.

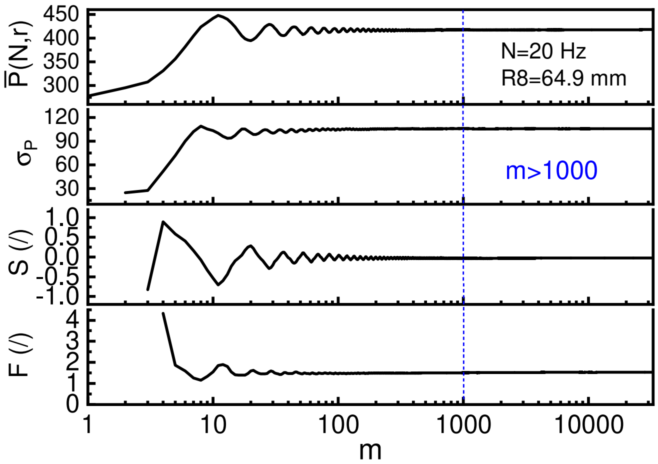

Fig. 9 Statistical convergence of raw data.

The standard deviation (σ_P) of fluctuating pressure versus mixing rate and radius is shown in Fig. 10a. It is interesting to find that the variation is highly dependent on the mixing rate. The maximum fluctuation occurs in the range of mixing rate from 15 to 30 Hz. And the fluctuating pressure strongly increases with a higher radius when $r>54$ mm. In contrast, at other mixing rates, these deviations are limited to less than 20 mbar.

The filtration performance can be described by Darcy's law, as displayed in Eq. (22). In dynamic filtration, membrane fouling is controlled by the local shear stress at the membrane surface, limiting the increase in total hydrodynamic resistance (R_h). The pursuit of higher permeate flux requires to apply optimal operating conditions by considering the continuous and fluctuating contributions of transmembrane pressure and their radial distribution over filtration surface. Most of the time, transmembrane pressure was given as the mean value. Another contribution of the driving force is the fluctuating pressure, which has not been reported in the literature, whereas its contribution cannot be neglected. In Fig. 10b, the fluctuating component (σ_P) constitutes more than 10% of transmembrane pressure at 20 Hz for most of the radius, even reaching 25.3% at R8. The grey area (15 to 30 Hz) will be a good choice to intensify the fluctuating magnitude. Thus, as the maximum σ_P reach 100 mbar, a minimum counter pressure of 300 mbar ($3\sigma_P$) will be requested to avoid membrane detachment. Similar to ΔP_{mixing}, a semi-empirical correlation to describe σ_P will be useful to estimate local transmembrane pressure.

$$J(N,r,t) = \frac{\bar{P}(N,r) + \tilde{P}(N,r,t)}{\mu R_h} \tag{22}$$

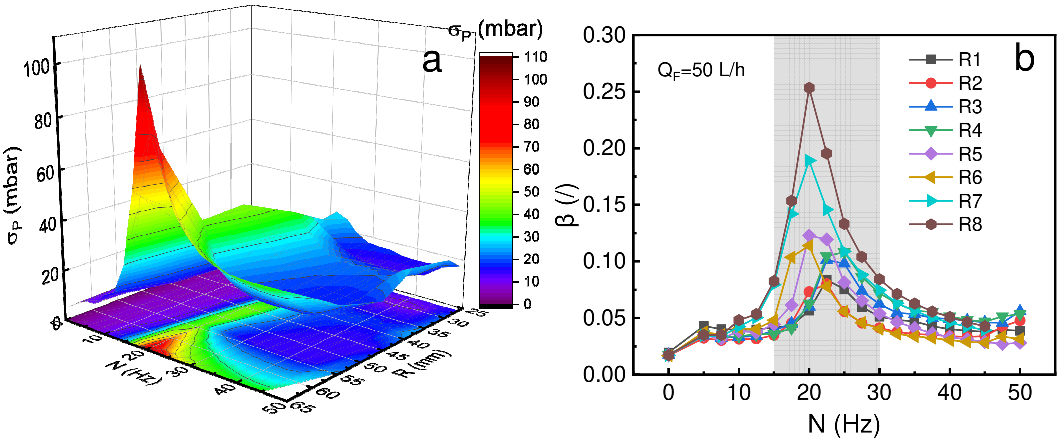

Fig. 10 Statistic analysis. (a) the standard deviation of fluctuating pressure at different mixing rate and radius; (b） the coefficient of variation versus mixing rate.

The skewness distribution of fluctuating pressure at different conditions are given in Fig. 11a. The skewness number varies from -0.3 to 0.3, showing a good symmetry of the distribution. The flatness indicates the degree of peakedness of distribution and displayed in Fig. 11b. It is concluded that the flatness increases as the mixing rate applied below 7.5 Hz, and followed by a decrease until 20 Hz. The relative lower mixing rate results in flatness maintain in the range from 5 to 35, which means the excessive sharpness of PDF. Above 20 Hz, most cases ($r>45.3$ mm) give the flatness inferior to 3, which indicates the great extension of PDF to large fluctuating amplitude. However, a small increase of F can be observed at a lower radius ($r<45.3$ mm). Furthermore, the flatness decreases with increasing radius at the same mixing rate. At 20 Hz, F reaches its minimum value, corresponding to the maximum fluctuating pressure. Centred moments such as skewness and flatness are known for normal and sinusoid wave distributions but can hardly be compared with experimental data. Skewness is not significant due to symmetric distribution. Flatness appears as an appropriate qualitative criterion to discriminate the fluctuating contribution as a function of the mixing rate.

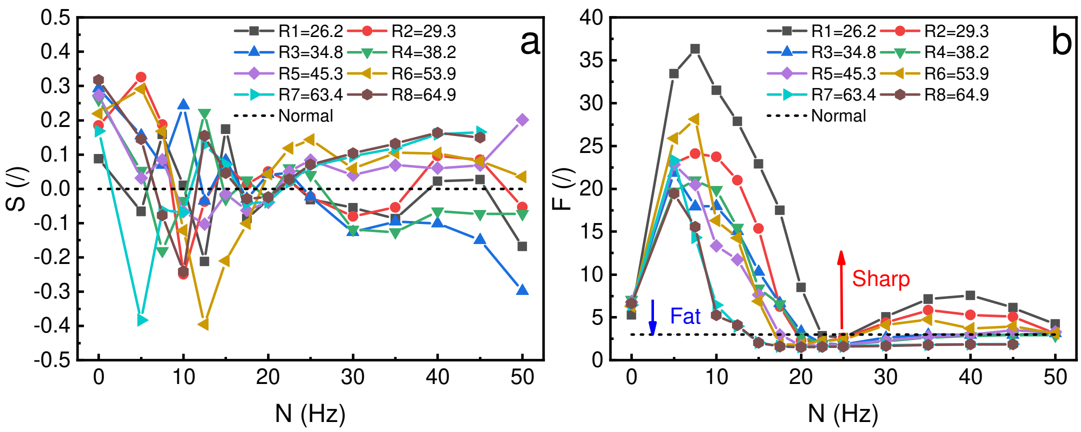

Fig. 11 The skewness and flatness distribution at different radius

3.3.2 Probability distribution function

Fig. 12a shows the probability distribution of fluctuating pressure from 0 to 50 Hz at R6. When the mixing rate is below 10 Hz, the spectrum displays as unimodal, confined to a narrow fluctuating signal. When *N>10* Hz, the peak at the zero deviations sinks downward and expands to the sides, forming a bimodal and reaching the highest deviation at 20 Hz. Nevertheless, The PDF at 10, 40 and 45 Hz can be defined as the transition zone. In general, the probability distribution of a sinusoidal signal has a U-shaped structure, while a random signal tends to be normally distributed. The transition from unimodal to bimodal will occurs with the increased contributions of the sinusoidal wave relative to the random component.

Considering the peak-to-peak values in Fig. 12b, the fluctuating pressure evolves with the mixing rate and radius. The unimodal region occurs below 10 Hz, whose amplitude cannot be achieved due to only one peak value observed. The dash lines demonstrate the transition areas in the range from 10 to 17.5 Hz and 30 to 50 Hz. However, at a large radius, such as R8, the intensive fluctuation (bimodal) happens at *N>10* Hz and reaches the maximum peak-to-peak value of 144 mbar at 20 Hz.

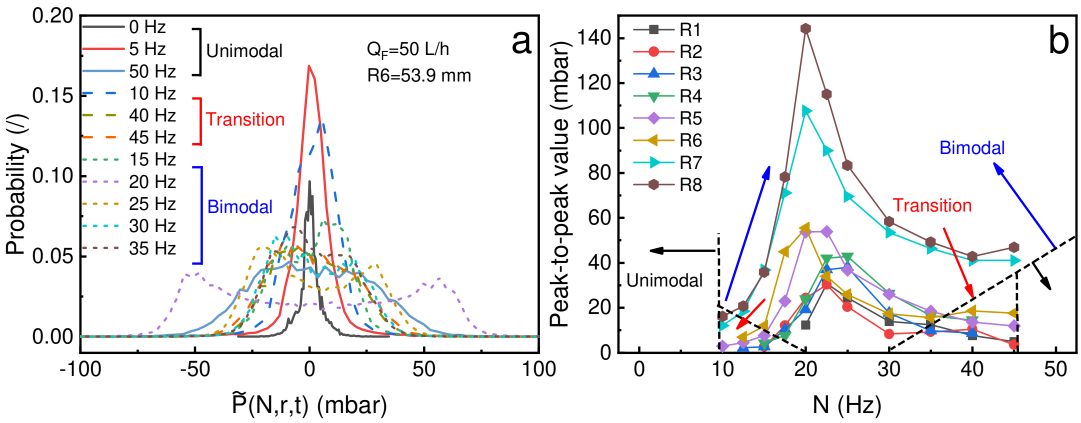

Fig. 12 PDF analysis. (a) the probability distribution of fluctuating pressure at R6; (b) the evolution of PDF width (peak-to-peak/2) versus mixing rate.

3.3.3 Fast Fourier transform

Statistical analysis and probability distribution function provides a global overview of fluctuating pressures in the time domain. However, the characterisation and decomposition of the signal primarily rely on frequency domain analysis. Empirical Mode Decomposition (EMD) decomposes the signal into Intrinsic Mode Functions (IMF). Then, via the Hilbert Transform, the instantaneous frequency of the data is properly identified, commonly used in the analysis of non-stationary and non-linear signals [26, 35]. For periodic signals, frequencies remain constant over the time range, and hence the FFT is preferred [28, 30].

After FFT, the periodic signal generated by mixing with a three-blade impeller includes the main contributions of the sinusoidal wave at *N*, *2N*, *3N*, *4.25N* and *6N*. Fig. 13a shows that the amplitudes for each component vary as *N* increase. The cumulative amplitude at 20 Hz tends to be the highest and followed by 17.5 and 22.5 Hz, which constitute the most intensive fluctuation. Below 10 Hz, the amplitude consists of two main parts: *3N* and *6N*, but each of them is lower than 3 mbar. Increasing the mixing rate, other fluctuating contributions can be observed, especially a small increase of amplitude at *N* after 20 Hz. It should be noted that *3N* shows to be the most important wave from 60% up to 90% at 17.5 and 20 Hz.

In Fig. 13b, the main contribution of amplitudes ($f=3N$) is plotted as a function of mixing rate. The sharp increase of amplitude is found below 20 Hz, then fall to a constant value between 20 and 30 Hz. Above 30 Hz, the increase of mixing rate has little effect. It is likely that the amplitude increases with the radius, especially at $r>53.9$ mm. However, the amplitude evolution almost follows the same curve for R7 and R8, which is different from σ_p (Fig. 10a) and PDF amplitudes (Fig. 12b).

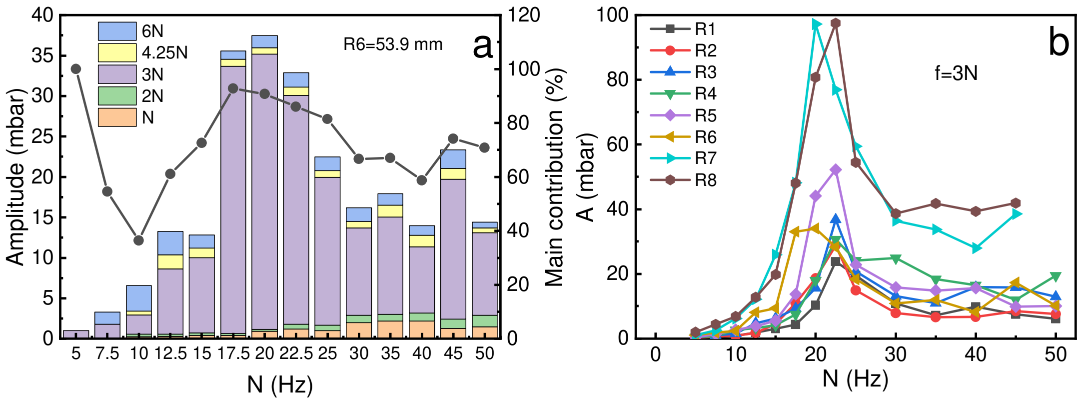

Fig. 13 Frequency domain analysis. (a) Evolution of cumulative amplitude from FFT versus mixing rate at R6; (b) the amplitude at 3N versus mixing rate and radial position.

3.3.4 Model of fluctuating component and associated energy input

Modelling and quantifying periodic and random contributions of fluctuating pressure have been determined by identifying amplitude, *A* and standard deviation, σ (cf. §2.3.4). The total energy input and the weight of the periodic part are given by the sum of periodic ($A/\sqrt{2}$) and random (σ) intensities, and the ratio between periodic and total energies ($\frac{R}{P+R}=\frac{A/\sqrt{2}}{A/\sqrt{2}+\sigma}$), respectively. In Fig. 14a, the total energy evolves with radius and mixing rate. It is interesting to find that a rectangular area ($17.5<N<25$ Hz and $34.8<r<64.9$ mm) corresponds to the extensive energy input over 40 mbar. In addition, the same zone can be observed at $r>53.9$ mm and $17.5<N<45$ Hz. It includes the maximum energy of more than 100 mbar at 20 Hz for R8.

For the random signal, the standard deviation varies in the range from 5 to 22 mbar. While the amplitude for the periodic signal changes from 1 to 107 mbar, and is highly dependent on the mixing rate and radius. Fig. 14b shows the map of the ratio between periodic and total energy input for the fluctuating pressure. It indicates that periodic signal is dominant for most cases and contributes to more than 60% in a trapezoidal area from 12.5 to 45 Hz. The maximum ratio happens between 15 and 30 Hz, which is the same as the intensive fluctuation area given by statistical analysis.

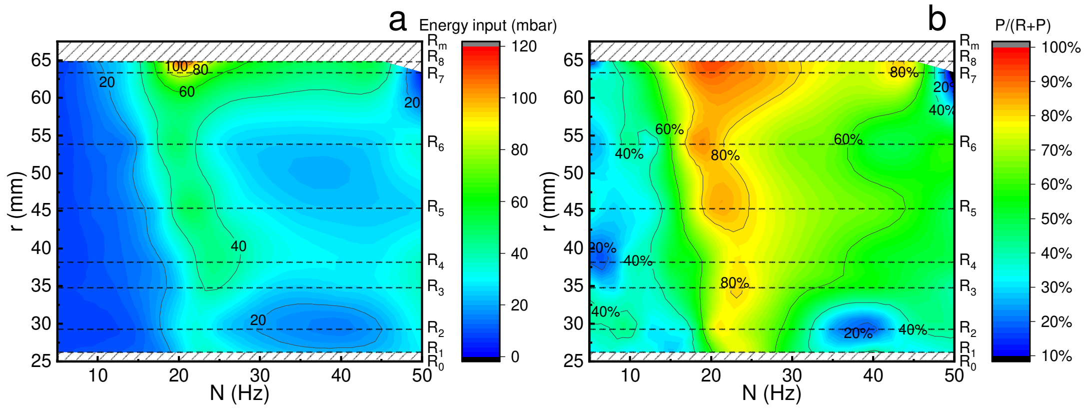

Fig. 14 Spectrum of total energy input and periodic contribution as a function of mixing rate and radius

3.3.5 Comparison of fluctuating intensity

Table 3 Information on the data treatment

Method	Mean pressure	Fluctuating pressure		
		Periodic + Random	Periodic	Random
SA	$\bar{P}(N,r)$	σ_p, S, F	/	/
PDF	/	*Peak-to-peak*	/	/
FFT	/	/	A_i, f_i	/
Model	/	/	A_1, f_1	σ

The evolution of fluctuating pressure for three strategies and modelling are compared in Fig. 15. From a global perspective, the deviations of the curves almost share the same trends with increasing mixing rate. The results from PDF are higher than other methods, around 1.04 (±0.17) times of σ_p above 15 Hz. Nevertheless, the former case contains information about fluctuations in all ranges, which can be useful in signal reconstruction. Meantime, the amplitude from FFT at 3N indicates 0.72 (±0.18) times of σ_p. This ratio increases to 0.9 if the contribution of other peaks (*N*, *2N*, *4.25N* and *6N*) are considered. When it comes to the model, fluctuation intensity is composed of the period and random contributions. The total energy input is higher than σ_p and reaching 126%. As shown as a grey zone in Fig. 15, the intensive fluctuation occurs in the range from 15 to 30 Hz.

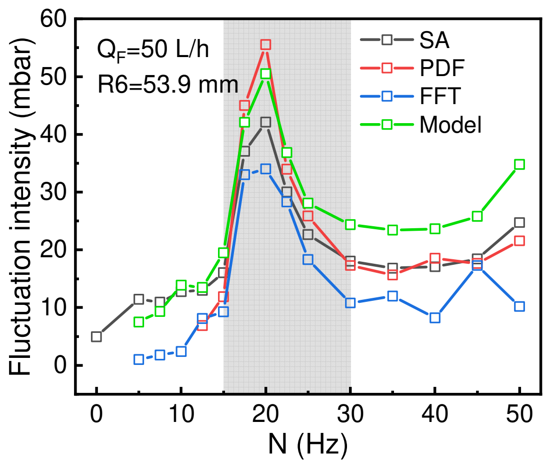

Fig. 15 The evolution of pressure deviations (standard deviation, peak-to-peak/2, amplitude from FFT at 3N and total energy for modelling) as a function of mixing rate at R6.

4 Conclusions

Dynamic filtration enables to reduce fouling and to enhance permeate flux by a mechanical movement with rotating oscillating and/or vibrating. These mechanical configurations generate complex flow pattern with local fluctuation at the membrane surface. Therefore, the hydrodynamics within the filtration unit needs to be investigated from a global up to a local and instantaneous standpoint in order to understand the filtration performances. The present work introduces the methodology to investigate instantaneous and local transmembrane pressure within Rotating and Vibrating Filtration (RVF) module under a turbulent regime. A preliminary global approach is based on classical mixing power and pressure drop measurements; then, semi-local and local approaches interpret and describe local and instantaneous pressure at the membrane surface using alternative strategies.

From global and semi-local approaches, friction and mixing power in the RVF module are described by semi-empirical correlations based on mixing and feeding conditions. The generalised correlations between Euler and mixing effect ($Re_{mixing}/Re_{feeding}$) are proposed to estimate the pressure drop. Pumping power can be easily achieved with feeding and back pressure; it demonstrates that the power for feeding can be neglected compared with mixing over 20 Hz. The balance between heat dissipation and net mixing power exhibits an accurate linear relation (slope=0.88). However, the calculated power based on the shear of the impeller surface is strongly underestimated. The major effect of pressure driving force between the leading and trailing edge at the blades needs to be specified.

The semi-local approach contributes to estimate and model the continuous component of the filtration driving force ΔP_{mixing}. The evolution of mixing pressure depends mainly on radius and mixing rate, rarely on flowrate. Due to the radial velocities generated by feeding flowrate, the integration of mixing pressure with N^2r^2 yields the experimental core velocity coefficient k_{exp} superior to the theoretical value k_{theo}. The great contribution of radial velocity on the k_{exp} can be observed at the lowest radius R1 and increase with flowrate, but decrease with mixing rate and radius. The ratio between radial and angular velocity is easily determined by simple correlations in the rotating disk system, which can be extended to the conditions of the rotating impeller. However, the reason for the small increase in k value at a large radius ($r>45$ mm) is not clear.

Instantaneous and local pressure at the membrane surface was deeply scrutinised by comparing analytical methodology (SA, PDF, FFT and modelling) in order to understand and to estimate the fluctuating component of driving force. The intensive fluctuation area for three methods appears in the same range of mixing rate from 15 to 30 Hz, and increase with the radial position. The important contribution of fluctuating pressure shows great potential for large-scale application. On frequency domain, the prominent peaks of FFT include N, $2N$, $3N$, $4.25N$ and $6N$, where the amplitude at $3N$ is indicated as the dominant position (from 60 up to 97%). The modelling can be established by the random signal and sinusoid wave ($f=3N$), which related to the PDF evolution from unimodal (random) to bimodal (periodic) with mixing rate. It can be concluded that the periodic component is more sensitive to the mixing rate relative to the random part.

Future works will apply this methodology to compare and to screen different impellers (design and selection). This strategy can be extended to the laminar regime with Newtonian and Non-Newtonian fluids. The measurement and analysis of instantaneous and local pressure stood as a knowledge gap to understand the performances of the dynamic filtration module. In this aim, the instantaneous and local wall shear rate could be investigated by local measurements at the membrane surface (electrochemical technique) and compared with velocity field (PIV, particle image velocimetry).

Nomenclature

a, b	Numerical coefficient, /
A	Amplitude, mbar
C_P	Specific heat capacity, J/(kg·°C)
d	Diameter of inlet tube, m
d_i	Diameter of impeller, m
$E_P(x)$	Periodic PDF, mbar^{-1}
$E_R(x)$	Random PDF, mbar^{-1}
Eu	Euler number, /
F	Flatness, /
f	Frequency, Hz
J	Permeate flux, m^3/(m^2·s)
k	Core velocity coefficient, /
m	Sampling number, /
N	Mixing rate, Hz
Np	Power number, /
P_0	Pressure without mixing, mbar
P_f	Power consumption without load, W
$P_P(t)$	Periodic signal, mbar
$P_R(t)$	Random signal, mbar
$P(N,r,t)$	Instantaneous pressure, mbar
$\bar{P}(N,r)$	Mean time pressure, mbar
$\tilde{P}(N,r,t)$	Deviated pressure, mbar
Q_F	Feeding flowrate, m^3/s
R_0	Inner radius of impeller, m
R_h	Total hydrodynamic resistance, m^{-1}
R_i	Impeller radius, m
r	Radius at the membrane surface, m
$Re_{feeding}$	Feeding Reynolds number, /
Re_{mixing}	Mixing Reynolds number, /
S	Skewness, /
s	Gap between the rotor and membrane, m
T_{inlet}	Inlet temperature, °C
T_{outlet}	Outlet temperature, °C
U_r	Radial velocity, m/s
U_θ	Tangential velocity, m/s
$U_{r\theta}$	Horizontal velocity, m/s
u	Fluid velocity, m/s
τ	Shear stress, Pa
β	Coefficient of variation, /
γ	Shear rate, s^{-1}
ρ	Fluid density, kg/m^3

σ	Standard deviation of random signal, mbar
σ_P	Standard deviation of fluctuating pressure, mbar
μ	Fluid dynamic viscosity, Pa·s
Φ_M	Mechanical power, W
Φ_N	Net electrical power, W
Φ_T	Thermal dissipation, W
ΔP_{RVF}	Pressure drops of RVF module, mbar
ΔP_{mixing}	Additional pressure generated by mixing, mbar

Acknowledgements

Financial support from the China Scholarship Council (CSC) for Ming CHENG (grant No. 201801810069) is gratefully acknowledged. Thanks to Pascal DEBREYNE and Jacky SIX (INRAE, Lille) for the realisation of the experimental device about the instantaneous and local pressure measurement.

References

[1] M.M. Pendergast, E.M. Hoek, A review of water treatment membrane nanotechnologies, Energy & Environmental Science, 4 (2011) 1946-1971.

[2] F. Lipnizki, Cross-flow membrane applications in the food industry, Membrane Technology: Membranes for food applications, 3 (2010) 1-24.

[3] M. Selvamuthukumaran, Applications of Membrane Technology for Food Processing Industries, CRC Press, 2020.

[4] E. Drioli, L. Giorno, Biocatalytic membrane reactors: applications in biotechnology and the pharmaceutical industry, CRC Press, 2020.

[5] M.Y. Jaffrin, Dynamic filtration with rotating disks, and rotating and vibrating membranes: an update, Current Opinion in Chemical Engineering, 1 (2012) 171-177.

[6] L. Ding, M.Y. Jaffrin, J. Luo, Dynamic Filtration with Rotating Disks, and Rotating or Vibrating Membranes, (2015) 27-59.

[7] R. Bouzerar, M. Jaffrin, L.-H. Ding, P. Paullier, Influence of Geometry and Angular Velocity on Performance of a Rotating Disk Filter, AIChE Journal, 46 (2000) 257-265.

[8] L. Fillaudeau, B. Boissier, A. Moreau, P. Blanpain-Avet, S. Ermolaev, N. Jitariouk, Investigation of rotating and vibrating filtration for clarification of rough beer, Journal of Food Engineering, 80 (2007) 206-217.

[9] L. Fillaudeau, B. Boissier, S. Ermolaev, N. Jitariouk, Etude hydrodynamique d'un module de filtration dynamique, Ind. Alim. Agri., 124 (2007) 8-16.

[10] O.A. Akoum, M.Y. Jaffrin, L. Ding, P. Paullier, C. Vanhoutte, An hydrodynamic investigation of microfiltration and ultrafiltration in a vibrating membrane module, Journal of Membrane Science, 197 (2002) 37-52.

[11] X. Xie, C. Le Men, N. Dietrich, P. Schmitz, L. Fillaudeau, Local hydrodynamic investigation by PIV and CFD within a Dynamic filtration unit under

laminar flow, Separation and Purification Technology, 198 (2018) 38-51.

[12] M.Y. Jaffrin, L.-H. Ding, O. Akoum, A. Brou, A hydrodynamic comparison between rotating disk and vibratory dynamic filtration systems, Journal of Membrane Science, 242 (2004) 155-167.

[13] M. Frappart, M.Y. Jaffrin, L.H. Ding, V. Espina, Effect of vibration frequency and membrane shear rate on nanofiltration of diluted milk, using a vibratory dynamic filtration system, Separation and Purification Technology, 62 (2008) 212-221.

[14] L. Ding, O. Al-Akoum, A. Abraham, M.Y. Jaffrin, Milk protein concentration by ultrafiltration with rotating disk modules, Desalination, 144 (2002) 307-311.

[15] L. Li, L. Ding, Z. Tu, Y. Wan, D. Clausse, J.-L. Lanoisellé, Recovery of linseed oil dispersed within an oil-in-water emulsion using hydrophilic membrane by rotating disk filtration system, Journal of Membrane Science, 342 (2009) 70-79.

[16] A. Brou, L. Ding, P. Boulnois, M.Y. Jaffrin, Dynamic microfiltration of yeast suspensions using rotating disks equipped with vanes, Journal of Membrane Science, 197 (2002) 269-282.

[17] O. Al-Akoum, L. Ding, M. Jaffrin, Microfiltration and ultrafiltration of UHT skim milk with a vibrating membrane module, Separation and Purification Technology, 28 (2002) 219-234.

[18] M. Cheng, X. Xie, P. Schmitz, L. Fillaudeau, Extensive review about industrial and laboratory dynamic filtration modules: scientific production, configurations and performances, Separation and Purification Technology, (2021) 118293.

[19] J.W. Daily, R.E. Nece, Chamber dimension effects on induced flow and frictional resistance of enclosed rotating disks, (1960).

[20] H. Ketola, J. McGrew, Pressure, frictional resistance, and flow characteristics of the partially wetted rotating disk, (1968).

[21] L. Rudniak, S. Wroński, Influence of hydrodynamics of rotary dynamic filters on separation processes, Chemical Engineering & Technology: Industrial Chemistry-Plant Equipment-Process Engineering-Biotechnology, 18 (1995) 90-95.

[22] R. Bouzerar, M.Y. Jaffrin, A. Lefevre, P. Paullier, Concentration of ferric hydroxide suspensions in saline medium by dynamic cross-flow filtration, Journal of Membrane Science, 165 (2000) 111-123.

[23] L.O. Wilson, N.L. Schryer, Flow between a stationary and a rotating disk with suction, Journal of Fluid Mechanics, 85 (2006) 479-496.

[24] L.-H. Ding, O. Akoum, A. Abraham, M.Y. Jaffrin, High shear skim milk ultrafiltration using rotating disk filtration systems, AIChE Journal, 49 (2003) 2433-2441.

[25] L. Chen, Y. Qiu, Removal of Cd (II) from dilute aqueous solutions by complexation–ultrafiltration using rotating disk membrane and the shear stability of PAA–Cd complex, Chinese Journal of Chemical Engineering, 27 (2019) 519-527.

[26] H. Meng, W. Wang, J. Wu, Y. Yu, F. Wang, Experimental study on instantaneous pressure fluctuation time series in the novel tank agitated by multiple

horizontal jets, Chemical Engineering Research and Design, 90 (2012) 1750-1764.

[27] K. Hirata, Y. Iida, A. Takushima, J. Funaki, Instantaneous pressure measurement on a rotating blade of a cross-flow impeller, Journal of Environment and Engineering, 3 (2008) 261-271.

[28] Z. Wang, Z. Qian, J. Lu, P. Wu, Effects of flow rate and rotational speed on pressure fluctuations in a double-suction centrifugal pump, Energy, 170 (2019) 212-227.

[29] S.M. Okhovat-Alavian, J. Behin, N. Mostoufi, Investigating the flow structures in semi-cylindrical bubbling fluidized bed using pressure fluctuation signals, Advanced Powder Technology, 30 (2019) 1247-1256.

[30] C. Kang, H. Liu, Pressure fluctuation and surface morphology induced by the high-pressure submerged waterjet confined in a square duct, International Journal of Heat and Fluid Flow, 77 (2019) 134-143.

[31] X. Xie, Investigation of Local and Global Hydrodynamics of a Dynamic Filtration Module (RVF Technology) for Intensification of Industrial Bioprocess, in, INSA Toulouse, 2017.

[32] F. Johnsson, R. Zijerveld, J.v. Schouten, C. Van den Bleek, B. Leckner, Characterization of fluidization regimes by time-series analysis of pressure fluctuations, International journal of multiphase flow, 26 (2000) 663-715.

[33] S.A. Wassie, A. Zaabout, F. Gallucci, S. Cloete, M. van Sint Annaland, S. Amini, Detecting densified zone formation in membrane-assisted fluidized bed reactors through pressure measurements, Chemical Engineering Journal, 308 (2017) 1154-1164.

[34] R. Bouzerar, Filtration dynamique dans un module plan à disque rotatif : Application à des suspensions minérales, in, 1999, pp. 181 p.

[35] N.E. Huang, Z. Shen, S.R. Long, M.C. Wu, H.H. Shih, Q. Zheng, N.-C. Yen, C.C. Tung, H.H. Liu, The empirical mode decomposition and the Hilbert spectrum for nonlinear and non-stationary time series analysis, Proceedings of the Royal Society of London. Series A: Mathematical, Physical and Engineering Sciences, 454 (1998) 903-995.